Malitckaya, M.; Komsa, H. P.; Havu, V.; Puska, M. J.

Effect of Alkali Metal Atom Doping on the CuInSe2-Based Solar Cell Absorber

Published in:
Journal of Physical Chemistry C

DOI:
10.1021/acs.jpcc.7b03083

Published: 27/07/2017

Document Version
Publisher's PDF, also known as Version of record

Please cite the original version:
Malitckaya, M., Komsa, H. P., Havu, V., & Puska, M. J. (2017). Effect of Alkali Metal Atom Doping on the CuInSe2-Based Solar Cell Absorber. *Journal of Physical Chemistry C*, *121*(29), 15516-15528. https://doi.org/10.1021/acs.jpcc.7b03083

THE JOURNAL OF PHYSICAL CHEMISTRY C

Article

pubs.acs.org/JPCC

Effect of Alkali Metal Atom Doping on the $CuInSe_2$-Based Solar Cell Absorber

M. Malitckaya, H.-P. Komsa, V. Havu, and M. J. Puska*

COMP Centre of Excellence, Department of Applied Physics, Aalto University, P.O. Box 11100, 00076 Aalto, Finland

ABSTRACT: The efficiency of $Cu(In,Ga)Se_2$ (CIGS)-based solar cells can be markedly improved by controlled introduction of alkali metal (AM) atoms using post-deposition treatment (PDT) after CIGS growth. Previous studies have indicated that AM atoms may act as impurities or agglomerate into secondary phases. To enable further progress, understanding of atomic level processes responsible for these improvements is required. To this end, we have investigated theoretically the effects of the AM elements Li, Na, K, Rb, and Cs on the properties of the parent material $CuInSe_2$. First, the effects of the AM impurities in $CuInSe_2$ have been investigated in terms of formation energies, charge transition levels, and migration energy barriers. We found that AM atoms preferentially substitute for Cu atoms at the neutral charge state. Under In-poor conditions, AM atoms at the In site also show low formation energies and are acceptors. The migration energy barriers show that the interstitial diffusion mechanism may be relevant only for Li, Na, and K, whereas all the AM atoms can diffuse with the help of Cu vacancies. The competition between these two mechanisms strongly depends on the concentration of Cu vacancies. We also discuss how AM atoms can contribute to increasing Cu-depleted regions. Second, AM atoms can form secondary phases with Se and In atoms. We suggest a mechanism for the secondary phase formation following the PDT process. On the basis of the calculated reaction enthalpies and migration considerations, we find that mixed phases are more likely in the case of $LiInSe_2$ and $NaInSe_2$, whereas formation of secondary phases is expected for $KInSe_2$, $RbInSe_2$, and $CsInSe_2$. We discuss our findings in the light of experimental results obtained for AM treatments. The secondary phases have large energy band gaps and improve the morphology of the buffer surface by enabling a favorable band alignment, which can improve the electrical properties of the device. Moreover, they can also passivate the surface by forming a diffusion barrier. Overall, our work points to different roles played by the light and heavy AM atoms and suggests that both types may be needed to maximize their benefits on the solar cell performance.

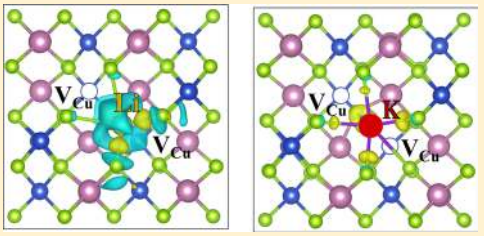

1. INTRODUCTION

The development of the chalcopyrite $Cu(In,Ga)Se_2$ (CIGS)-based solar cell devices started fully in the 1970s at Bell Laboratories. The efficiencies of the first solar cells were on the order of 12%. Since those times, the solar cell devices have been improved in several phases related to the different advances in the growth process and materials development[1−4] increasing the efficiency to the present record efficiency of 22.6% obtained at ZSW.[3]

The new high-efficiency CIGS films are typically grown by coevaporation of the individual elements on flexible plastic substrates[2] or on heated soda lime glasses (SLG).[5] In order to achieve high efficiencies, incorporation of alkali metal (AM) atoms in the so-called post-deposition treatment (PDT) is required in both processes,[6,7] although when using the SLG substrate Na and to a lesser extent also K diffuse from the substrate into the CIGS absorber layer.[1,8] In the PDT process, alkali fluorides are evaporated on top of the absorber layer under a selenium atmosphere. The resulting Na and K concentrations in the absorber layer are typically about 0.1%.[2] The effect of Na and K PDT as well as that of Rb and Cs on the electronic properties of the CIGS material was recently investigated experimentally.[2,3] The positive effect of Na is understood to follow from the increase of the p-type conductivity and the ensuing increase in the open-circuit voltage.[2] K improves also the surface morphology, allowing thinner CdS buffer layers with smaller optical losses.[9] The above-mentioned record efficiency of 22.6% was obtained by Jackson et al. by applying Rb-PDT to absorbers on SLG. However, in spite of the extensive research, the microscopic origin of the efficiency improvement is still unknown.[3]

Atom probe tomography (APT) has revealed that regardless of the doping method, AM atoms accumulate preferably at the grain boundaries and near the absorber surface.[10−12] Several experiments[2,7,13,14] have pointed out that these regions become simultaneously Cu-depleted. The existence and the increase of Cu-depleted regions can be explained by the out-diffusion of Cu atoms and in-diffusion of AM atoms.[9] This was also proposed to underlie the increased p-type conductivity after Na PDT.[15,16] At an elevated PDT temperature Na atoms may substitute for Cu atoms in the bulk absorber. Afterward, at a lower temperature, Na atoms diffuse to the absorber surface because of the low Na solubility. The resulting Cu vacancies lead to increased p-doping. Information about AM diffusion can be obtained from X-ray photoelectron spectroscopy (XPS),[17] secondary ion mass spectroscopy (SIMS) measurements,[2] and

Received: March 31, 2017
Revised: June 9, 2017
Published: July 7, 2017

DOI: 10.1021/acs.jpcc.7b03083
J. Phys. Chem. C 2017, 121, 15516−15528

SIMS combined with APT.[18] The measured activation energies for Na inside the CIGS grains are low, 0.32,[19] 0.36,[18] and 0.37 eV,[17] which enables their efficient diffusion during the PDT.

Several experimental and theoretical works associate the positive effect of AM doping of the CIGS absorber with the formation of secondary phases.[2,15,20] The binding of Na atoms after Na deposition to the CIGS surface has been investigated experimentally by Klein et al.[21] This XPS experiment revealed formation of the Na_2Se phase during Na deposition. On the other hand, phases containing K, In, and Se have been found simultaneously with In_2Se_3 on top of the CIGS layer.[22] The existence of Na_2Se, K_2Se, and $NaInSe_2$ phases has also been predicted theoretically.[15,20]

The electronic effects of Li, Na, and K on the $CuInSe_2$ have already been investigated by first-principles modeling based on the density functional theory (DFT).[15,20,23,24] The calculations show that Li, Na, and K occupy preferably Cu sites as substitutional neutral impurities or positively charged impurity pairs, but they do not reveal any direct way how Li-, Na-, and K-related defects could affect the p-type doping or the efficiency of the CIGS solar cells. Moreover, the identification of the most abundant impurity configurations depends strongly on whether the elemental AM phases or secondary phases are used to determine the AM chemical potentials. To the best of our knowledge, no calculations for Rb and Cs impurities have been reported to date.

DFT modeling has also been used to study the diffusion of AM impurities in $CuInSe_2$.[15,23] The vacancy mechanism for Na diffusion in the bulk has been suggested to dominate the interstitial migration mechanism, because the migration barrier (0.3−0.35 eV)[15,23] of the substitutional Na to the neighboring Cu vacancy is lower than that for an interstitial Na (0.5 eV).[23] The model based on vacancy migration barriers is supported also by the experimental observation that a large concentration of Cu vacancies accumulates close to the surface and forms with In_{Cu} antisites ordered defect compounds (ODCs).[25,26] Oikkonen et al. note also that after a Na atom has substituted for a Cu atom, the Cu atom may diffuse using the interstitial mechanism with a migration barrier of only 0.2 eV.[27] Thus, on the atomic level, there would be two diffusion fluxes in opposite directions. According to Maeda et al., Li and K prefer to diffuse via the vacancy mechanism, with migration energies of 0.61 and 0.25 eV, respectively.[15] The diffusion mechanisms for other AM impurities, as well as their migration barriers, are poorly understood.

In this work, we present a comprehensive modeling study on the behavior of AM atoms in the $CuInSe_2$ absorber layer during PDT to fill in gaps in the existing knowledge and provide a consistent set of results. We have employed DFT calculations within the hybrid functional scheme. We have calculated formation energies of AM-related point defects, such as different substitutional impurities and interstitials, as well as dumbbells substituting Cu. Moreover, in order to understand the evolution of AM distributions during the PDT, migration barriers for AM impurities have been determined for the vacancy and interstitial diffusion mechanisms. The migration barriers show nonlinear trends along the AM column from Li to Cs, which are due to a decrease in the tendency for bond forming along an increase of the ionic size.

In addition, the feasibility of secondary phase formation has been investigated. A mechanism for the secondary phase formation during the PDT process is suggested, on the basis of calculated heats of formation. Finally, we have calculated the properties of the secondary phases. The results support the notion that the formation of secondary phases may be responsible for changes in the electronic structure and the morphology of the absorber layer.

The structure of the paper is as follows. Computational methods are described in the Computational Details section. Chemical potentials determined for AM atoms under different growth conditions, the ensuing formation energies of AM-related point defects, and the migration barriers are given and discussed in the Alkali Metal Impurities section. We give a short conclusion about AM incorporation into the absorber layer in the section titled Alkali Metal Incorporation into the Absorber Layer. The formation and properties of secondary phases are dealt with in the Secondary Phases section. Conclusions about the competition between formation of secondary phases and formation of impurities are given in the Secondary Phases vs Impurities section. The results are summarized and discussed in the Conclusions section.

2. COMPUTATIONAL DETAILS

The impurity formation energies for AM atoms were derived from the equation[28]

$$E_{f,i} = E^{def}_{tot,i} - E^{bulk}_{tot} - \sum_j n_j\mu_j + q(E_f + E_v) + E_{corr} \quad (1)$$

where $E^{def}_{tot,i}$ is the total energy of a supercell with the AM impurity of type i, E^{bulk}_{tot} is the total energy of the corresponding pristine supercell, μ_j is the chemical potential of the atom of type j, q is the charge state of the impurity, E_f is the Fermi level measured from the valence band maximum (VBM) E_v, and E_{corr} is a correction to artificial electrostatic interactions arising from the supercell approximation.

The defect concentrations in the dilute limit are then evaluated simply from

$$c_i \simeq \exp(-E_{f,i}/k_BT) \quad (2)$$

where k_B is the Boltzmann constant and T is the operating temperature. It yields the concentrations per relevant lattice site types. In order to estimate only the order of magnitude, we do not consider the geometry-related prefactor or the entropy related to ionic vibrations.

The total energy calculations were carried out in the framework of DFT, using the VASP program package.[29,30] In our recent work, we presented a careful investigation into the role of various computational parameters for accurately predicting properties of native point defects in $CuInSe_2$.[31] For the present work, we adopted the same computational parameters. In particular, defects were modeled using a 128-atom supercell, which is sufficiently large to prevent significant wave function overlap and also to reduce the spurious electrostatic errors in the case of charged defects. The latter were efficiently corrected by using the method proposed by Freysoldt et al.[32,33] To improve the calculated band gap and to reduce the self-interaction error, the Heyd−Scuseria−Ernzerhof (HSE06) hybrid functional was used, with the standard mixing and screening parameters.[34] A plane wave cutoff energy of 455 eV was used and the Brillouin-zone integration was performed with a 2 × 2 × 1 Γ-centered k-point mesh.

To be consistent with the defect calculations, heats of formation, and consequently chemical potentials, of the competing phases were also calculated using the HSE06

DOI: 10.1021/acs.jpcc.7b03083
J. Phys. Chem. C 2017, 121, 15516−15528

functional with similar plane wave cutoffs and converged *k*-point meshes, which depend on the sizes of the primitive cells.

The calculations for migration barriers of AM impurities in the absorber layer were carried out by using the climbing image nudged-elastic-band method (CI-NEB).[35] Due to the computational cost, these calculations were performed using a smaller 64-atom supercell with the 4 × 4 × 4 *k*-point set. Moreover, the CI-NEB optimization was done with the PBE exchange–correlation functional, but the energies for the initial, the saddle point, and the final geometries were then recalculated using the HSE06 functional.

3. RESULTS AND DISCUSSION

3.1. Alkali Metal Impurities. *3.1.1. Chemical Potential Diagrams of Alkali Metal (Indium) Selenides.* The defect formation energies (eq 1) and, consequently, their equilibrium concentrations depend sensitively on the chemical potentials of the elements. In the present work, we used the knowledge about the secondary phase formation to determine the chemical potentials of AM atoms, as well as all other elements. More detailed descriptions about the secondary phase formation and the properties of the different phases are given later in section 3.2.

The stability diagrams for the secondary phases of AM atoms were obtained by using the formation enthalpies of different AM compounds ($AlkInSe_2$ and Alk_2Se, where Alk denotes the different AM species), $CuInSe_2$, and In selenides, as compiled in Table 1. We note that the experimental values correspond to room temperature, whereas the calculations are for 0 K. While little experimental data are available, previous calculations have indicated that the HSE06 functional yields heats of formation generally in a good agreement with the experimental values.[31,36]

Table 1. Formation Enthalpies (in eV) of AM (Indium) Selenides Calculated Using the HSE06 Functional[a]

	ΔH_f	
	calcd (HSE06)	expt[37]
In_2Se_3	−2.99	−3.57
InSe	−1.28	−1.22
$CuInSe_2$	−2.38	−2.12
$LiInSe_2$	−4.05	
$NaInSe_2$	−3.73	
$KInSe_2$	−4.17	
$RbInSe_2$	−4.23	
$CsInSe_2$	−4.34	
Li_2Se	−4.19	
Na_2Se	−3.55	
K_2Se	−3.62	
Rb_2Se	−3.49	
Cs_2Se	−3.47	

[a]Experimental values, where available, are taken from ref 37.

On the basis of the results in Table 1, $NaInSe_2$ is less likely to form than other $AlkInSe_2$ compounds studied. Formation enthalpies (ΔH_f) of Na_2Se, K_2Se, Rb_2Se, and Cs_2Se (Alk_2Se) compounds are nearly similar, while that for Li_2Se indicates a higher stability.

The Alk–In–Se and Cu–In–Se stability diagrams are shown in Figure 1 and they illustrate the ranges of chemical potentials at which certain compounds are the most stable ones. Moreover, each point in, for example, the $AlkInSe_2$ stability region corresponds to a set of chemical potentials satisfying the thermodynamic equilibrium condition

$$\Delta\mu_{Alk} + \Delta\mu_{In} + 2\Delta\mu_{Se} = \Delta H_f(AlkInSe_2) \quad (3)$$

A boundary condition for each of the components is $\Delta\mu_i \leq 0$, where $\Delta\mu_i$ is the difference between the chemical potentials of the element in the compound and in the stable elemental phase.

The stability areas are nearly similar for $NaInSe_2$ and $LiInSe_2$ and then they increase toward $CsInSe_2$. This means that $KInSe_2$, $RbInSe_2$, and $CsInSe_2$ are stable over broader ranges of experimental conditions than $LiInSe_2$ and $NaInSe_2$. This is also evident from the calculated formation enthalpies. Previous investigations have suggested that Alk_2Se and $AlkInSe_2$ phases may be present at the absorber surface and at the grain boundaries.[2,15,20] This is in agreement with the calculated stability diagrams.

In order to cover different corners of the stable areas and thereby give a good indication of the attainable variations of the formation energies, we chose three different chemical potential sets for each of the $AlkInSe_2$ compounds, one corresponding the equilibrium with Alk_2Se and two with $AlkInSe_2$. The corresponding points on the $CuInSe_2$ stability diagram were also calculated. The cornerpoints are labeled as A, B, and C, and they are defined as follows.

Cornerpoint A: Se-Rich, Cu-Rich, In-Poor, Alk-Rich. We first adopted a Se-rich atmosphere. The equilibrium with Alk_2Se immediately determines the AM chemical potential, and for Cu, we chose the equilibrium with $CuInSe_2$ and Cu_2Se. The chemical potential of In was obtained from the equilibrium with $CuInSe_2$. Thus,

$$\Delta\mu_{Se} = 0$$
$$\Delta\mu_{Alk} = (\Delta H_f(Alk_2Se) - \Delta\mu_{Se})/2$$
$$\Delta\mu_{Cu} = (\Delta H_f(Cu_2Se) - \Delta\mu_{Se})/2$$
$$\Delta\mu_{In} = \Delta H_f(CuInSe_2) - \Delta\mu_{Cu} - 2\Delta\mu_{Se}$$

Cornerpoint B: Se-Rich, Cu-Poor, In-Rich, Alk-Poor. Next, we adopted again a Se-rich atmosphere. In addition, we assumed an equilibrium with $AlkInSe_2$ and $CuInSe_2$, which leads to a dependence between $\Delta\mu_{Alk}$ and $\Delta\mu_{Cu}$. To determine the Cu chemical potential, we first set In to be in equilibrium with $AlkInSe_2$ and In_2Se_3 and then applied the equilibrium condition with $CuInSe_2$. As a result,

$$\Delta\mu_{Se} = 0$$
$$\Delta\mu_{In} = (\Delta H_f(In_2Se_3) - 3\Delta\mu_{Se})/2$$
$$\Delta\mu_{Cu} = \Delta H_f(CuInSe_2) - \Delta\mu_{In} - 2\Delta\mu_{Se}$$
$$\Delta\mu_{Alk} = \Delta H_f(CuInSe_2) - \Delta H_f(AlkInSe_2) + \Delta\mu_{Cu}$$

Cornerpoint C: Se-Poor, Cu-Rich, In-Rich, Alk-Rich. In this case, the AM chemical potential is still obtained from the equilibrium with $AlkInSe_2$ and $CuInSe_2$. We took the conditions for Cu, In, and Se from the maximally In-rich point at the top-right corner of the $CuInSe_2$ stability area, which at the same time corresponds to Cu-rich and Se-poor conditions. Thus,

DOI: 10.1021/acs.jpcc.7b03083
J. Phys. Chem. C 2017, 121, 15516–15528

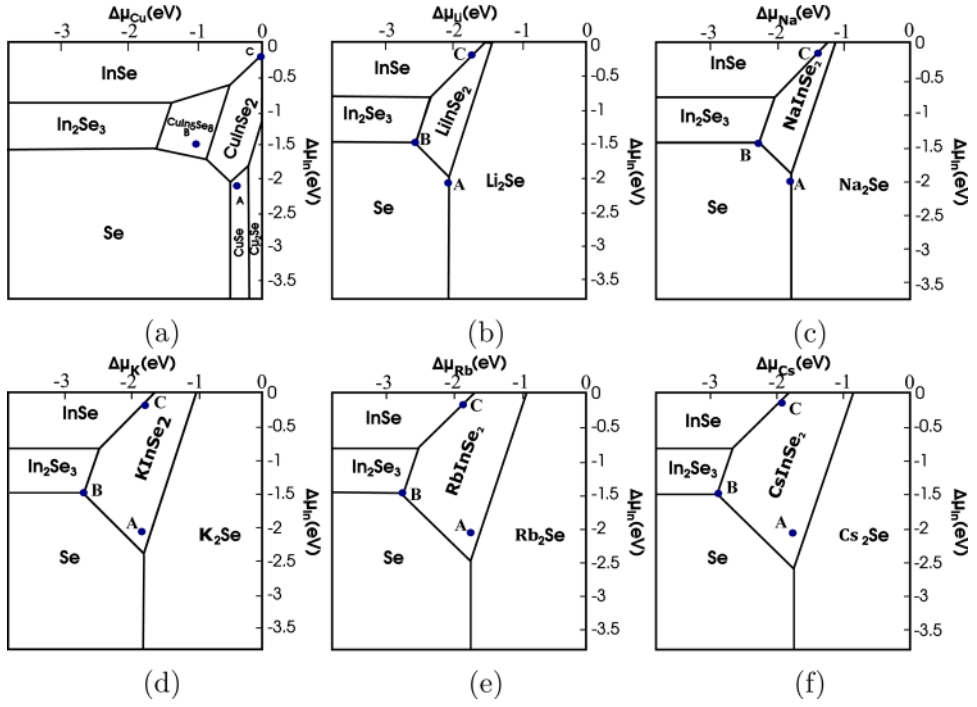

Figure 1. Stability diagrams for (a) Cu−In−Se, (b) Li−In−Se, (c) Na−In−Se, (d) K−In−Se, (e) Rb−In−Se, and (f) Cs−In−Se systems.

$$\Delta\mu_{Cu} = 0$$

$$\Delta\mu_{In} = -0.2 \text{ eV}$$

$$\Delta\mu_{Se} = \Delta H_f(CuInSe_2) - \Delta\mu_{Cu} - \Delta\mu_{In} = -1.07 \text{ eV}$$

$$\Delta\mu_{Alk} = \Delta H_f(CuInSe_2) - \Delta H_f(AlkInSe_2) + \Delta\mu_{Cu}$$

These chemical potential sets are also shown in Figure 1 within the Alk−In−Se stability diagrams and within the Cu−In−Se stability diagram.

3.1.2. Impurity Formation Energies. The formation energies of AM impurities calculated in this work are plotted in Figure 2 as a function of the Fermi energy. The results are shown for all the chemical potential sets A, B, and C discussed above (see Figure 1). Overall, the formation energy differences between Li and Na are smaller than 0.5 eV, after which the formation energies increase steadily from Na to Cs.

All the AM atoms prefer to accumulate on the Cu sublattice. This finding is largely independent of the chemical potential set chosen. Low formation energies for AM impurities on the Cu site can be associated with the weak covalent bond between the Cu and Se atoms.[38,39] AM atoms in the Cu sublattice are electronically inactive, neutral defects for all the Fermi level positions. Despite being neutral, by neutralizing the Cu vacancy acceptors, they can affect the charge carrier concentrations.

On the In site, all AM atoms behave as acceptors with charge states varying from 0 to −2, as could have been expected from a simple electron counting. The −2 charge state leads to a rapid decrease of the formation energies with the increasing Fermi energy, in which case In substitutions become even more stable than Cu substitutions. This is particularly true in the In-poor conditions A. Consequently, these defects produce one or two transition levels in the band gap, which can be detrimental to device properties. Here our results are in contrast with the previous results by Oikkonen et al.[23] and Ghorbani et al.[24] They predicted that Na_{In} produces just one transition level or has only one stable charge stage. The difference may be explained by the different supercell sizes and electrostatic correction schemes used. In most cases, the (0/−1) charge transition level is located more than 0.1 eV above the VBM, and thus, the defects cannot be classified as shallow acceptors. The only exception is Rb_{In}, for which we did not find a stable neutral charge state. While these defects can contribute to the increased p-type doping, it is worth noting that V_{In} is also an acceptor with the charge state varying from −1 to −3. Thus, if In vacancies are already present in the sample, filling them with AM atoms essentially leads to compensation by +1e and thereby to a reduced p-type doping.

AM atoms can also substitute Se. The formation energies for different AMs are similar, because of similar lattice relaxations in all cases. The substitutional Li_{Se} and Na_{Se} have formation energies higher than the other defects under all chemical conditions. K, Rb, and Cs might occupy Se sites under Se-poor conditions with formation energies comparable to those of AM impurities in the Cu site. However, the concentrations of these defects remain low because the formation energies of the substitutional atoms are more than 1.2 eV.

Furthermore, AM atoms, especially Li and Na, have small ionic radii and can accumulate on interstitial sites. We tested three possible sites and found that the tetrahedral configuration is the most stable configuration for Na, K, Rb, and Cs, whereas the octahedral configuration is more preferable for Li. The energy difference between the octahedral and tetrahedral positions increases with the size of the AM atom, because of the relaxation energy component. The (tetragonal) interstitial defects always have higher formation energies than AM atoms at the Cu site, but the difference remains roughly constant over the AM series. Our formation energies for the interstitial Na and K interstitial defects agree with the previous results by Oikkonen et al.[23] and Ghorbani et al.[24] As might be expected, the AM atoms can easily donate their lone s-electron and thus always exhibit the +1 charge state.

DOI: 10.1021/acs.jpcc.7b03083
J. Phys. Chem. C 2017, 121, 15516−15528

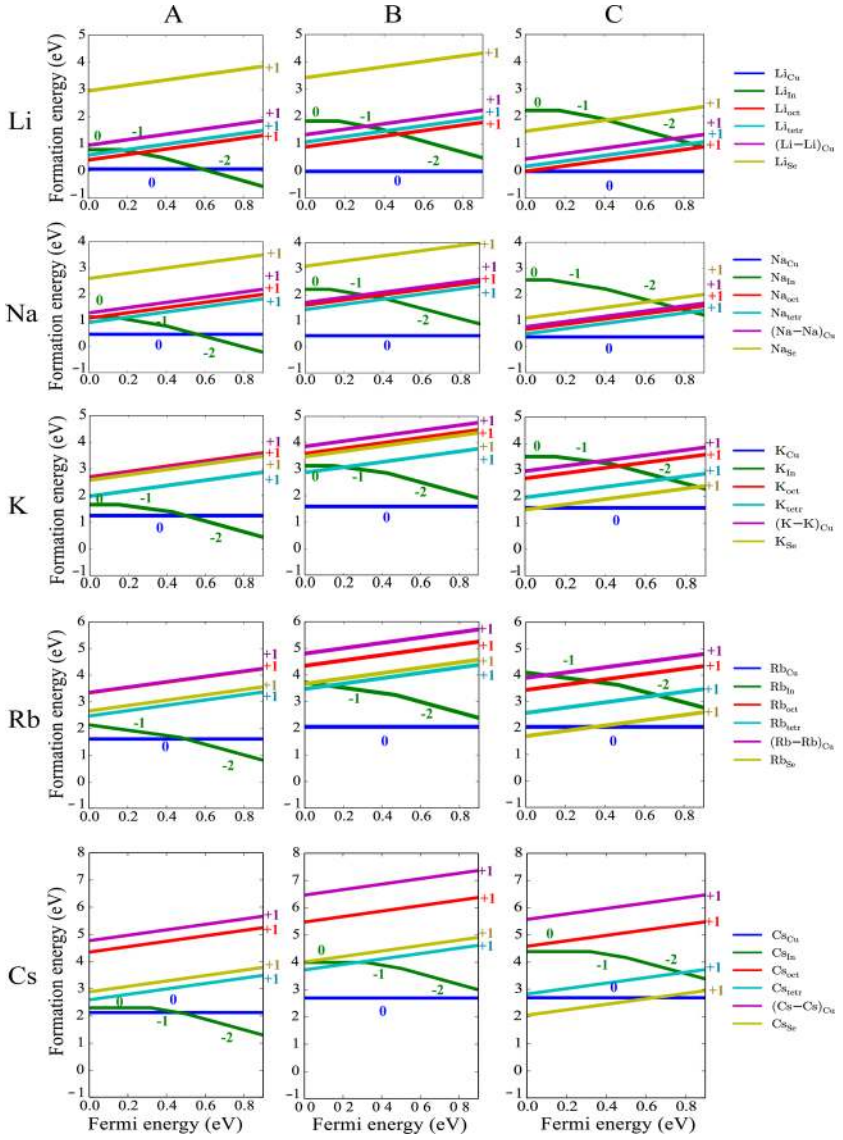

Figure 2. Formation energies for AM impurities. The formation energies for Li-, Na-, K-, Rb-, and Cs-related defects are given within the different panel rows. The formation energies corresponding to the points A, B, and C in Figure 1 are given within different panel columns: (A) Se-rich, Cu-rich, In-poor, Alk-rich; (B) Se-rich, Cu-poor, In-rich, Alk-poor; and (C) Se-poor, Cu-rich, In-rich, Alk-rich.

The dumbbell configurations of all the AM atoms act as donors, because their only stable states have the +1 charge. However, only the Li and Na dumbbells have formation energies low enough so that they could affect the electronic structure of $CuInSe_2$. This is in contrast to the findings by Oikkonen et al.[23] and Ghorbani et al.,[24] who found that dumbbells have very low formation energies. This is due to their choice of the AM chemical potentials taken from the elemental phases, whereas we have chosen to use the Alk_2Se or $AlkInSe_2$ phases, which should better correspond to the experimental conditions.

3.1.3. Impurity Migration Barriers. In order to better understand the rate at which AM atoms migrate inside the grains during the different PDT steps, knowledge of the relevant energy barriers for defect migration is required. In the present section we consider two diffusion mechanisms for AM atoms. In the vacancy mechanism, AM impurities, which we found to accumulate on the Cu sublattice, migrate to the nearest-neighbor Cu vacancy. The importance of the AM vacancy diffusion mechanism in the CIGS absorber layer has been underlined by several recently published theoretical works.[15,23] The second possibility is the migration of AM atoms via the interstitial mechanism. The elemental step of this mechanism is the jump of an AM atom from a tetrahedral position through an octahedral site to another tetrahedral position. The vacancy mechanism depends on the Cu vacancy concentration, and thus, the mechanism is sensitive to the Cu deficiency of the absorber layer.

Vacancy Diffusion Mechanism. The calculated migration barriers for the AM atoms from Li to Cs within the vacancy mechanism are shown in Figure 3. The migration barrier for Li is much higher than those for the other AM atoms, which likely reflects the low formation energy of the substitutional Li_{Cu} defect observed above. The obtained value of 0.63 eV is in a good agreement with the result by Maeda et al.[15] The migration barrier for Na is 0.32 eV, which fits well to the previous theoretical results by Oikkonen et al.[23] and Maeda et al.,[15] as well as to the experimental results.[17,18] For K, the migration barrier is 0.18 eV, i.e., still decreasing from the value for Na. A similar trend was observed by Maeda et al.[15] Rb has a migration

DOI: 10.1021/acs.jpcc.7b03083
J. Phys. Chem. C 2017, 121, 15516−15528

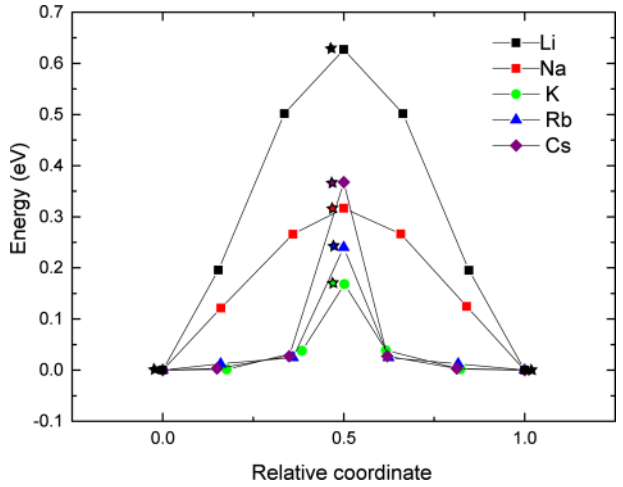

Figure 3. Migration barriers for Li, Na, K, Rb, and Cs within the vacancy diffusion mechanism. The PBE functional has been used in the CI-NEB calculation. The stars denote the barrier values calculated with the HSE06 functional using the atomic configurations determined by the PBE functional. The relative coordinates 0.0 and 1.0 correspond to neighboring vacancy sites and the relative coordinate 0.5 to the tetrahedral site in between.

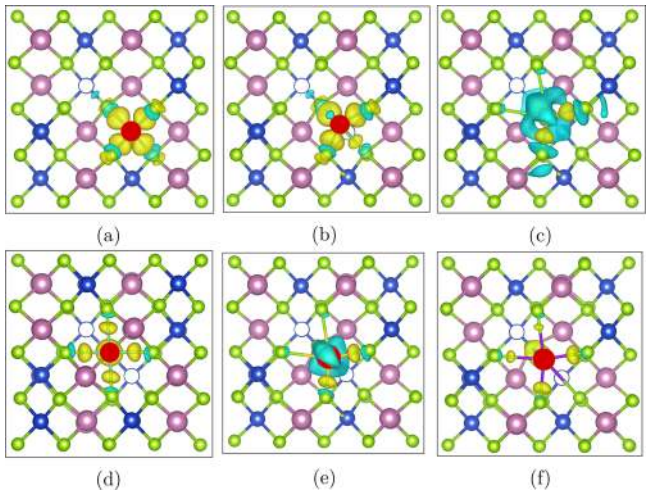

Figure 4. Electron density differences ($\Delta\rho$) defined in eq 4. (a) A Li atom starts from a Cu vacancy (coordinate 0.0 in Figure 3), (b, c) moves through two intermediate positions (coordinates around 0.16 and 0.34 in Figure 3), and (d) ends into the tetrahedral site (coordinate 0.5 in Figure 3) between the two Cu vacancies. (e) A Na and (f) a K atom in the intermediate position (coordinate around 0.34 in Figure 3). Yellow and blue isosurfaces correspond to the density accumulation and depletion, respectively. Blue, pink, green, and red spheres correspond to the Cu, In, Se, and AM atoms, respectively. White spheres denote Cu sites left vacant.

barrier of 0.24 eV, close to that of K, and Cs has a barrier of 0.37 eV, close to that of Na. Comparison with Figure 2 reveals that the barriers cannot be deduced simply from the formation energy difference between the alkali on the Cu site and on the tetragonal interstitial site.

Na, K, Rb, and Cs have migration barriers smaller than 0.4 eV, indicating rapid migration already at room temperature, i.e., much below the PDT temperature. The migration barrier is somewhat higher for Li, indicating modest diffusion at room temperature but significant diffusion at the PDT temperature.

For Li and Na, the migration barriers are wider than those for the three heavier AM elements considered. In order to understand the different shapes of the migration barriers for the light (Li and Na) and the heavy (K, Rb, Cs) AM atoms, as well as the trend in the barrier heights, we calculated electron density differences

$$\Delta\rho = \rho(\mathrm{CuInSe_2{+}Alk_{Cu}{+}V_{Cu}})^{-1} - \rho(\mathrm{Alk})^{+1} - \rho(\mathrm{CuInSe_2{+}2V_{Cu}})^{-2} \quad (4)$$

where $\rho(\mathrm{CuInSe_2{+}Alk_{Cu}{+}V_{Cu}})$, $\rho(\mathrm{Alk})$, and $\rho(\mathrm{CuInSe_2{+}2V_{Cu}})$ are the electron density of the $CuInSe_2$ host with a substituting AM atom and a neighboring Cu vacancy, an AM ion in vacuum, and the $CuInSe_2$ bulk with two Cu vacancies, respectively. The $(\mathrm{CuInSe_2{+}2V_{Cu}})$ system is calculated with the same geometry as the $(\mathrm{CuInSe_2{+}Alk_{Cu}{+}V_{Cu}})$ system, but without the AM atom. In eq 4, the charge states of different components are indicated and they show that the integrated electron density difference vanishes.

The electron density difference for the Li impurity, when it moves from the substitutional position to tetrahedral one, is shown in Figure 4. The substitutional Li makes strong bonds with the four nearest-neighbor Se atoms (Figure 4a). Then the Li atom moves out of the Cu site, which breaks a bond with one Se atom (Figure 4b). Energy is required to break the bond, and therefore, the Li energy barrier rises steeply in Figure 3 with the Li displacement from the Cu site.

The charge depletion region near the Li atom increases strongly toward the third position close to the tetrahedral site (Figure 4c). Due to changes in the charge distribution, the energy increases. Finally, in the tetrahedral site the Li ion has a tendency to create six bonds with the next-nearest-neighbor Se atoms (Figure 4d). However, these bonds are weak compared to those with the nearest-neighbor Se atoms in the Cu site and the migration barrier has a maximum in the tetrahedral site between the two Cu vacancies.

The behavior of the vacancy migration barrier for Na is similar to that for Li, but the barrier is lower than that for Li. In contrast, the K−Se bonds are weaker and there is no energy increase due to bond breaking when the K ion moves away from the Cu vacancy (Figure 4f). Therefore, the migration barrier does not rise until in close proximity of the tetrahedral site, where the Pauli repulsion between ion cores increases. The decrease of the migration barrier from Li to K reflects the decreasing tendency of these ions to form bonds with Se atoms in the $CuInSe_2$ host. The Na impurity exhibits a behavior similar to that of Li, but the bonds with Se atoms are weaker. This correlates with the smaller ionization potential of Na. When going further down in the AM row in the periodic table, the tendency toward bond making, as well as the ionization potential, decrease. After K the migration barrier increases to Rb and further to Cs. This reflects the increasing ionic radius and the ensuing increasing Pauli repulsion between the ion cores.

Interstitial Diffusion Mechanism. The migration barriers between two tetrahedral sites via an octahedral site in the $CuInSe_2$ chalcopyrite structure are shown in Figure 5. The migration barriers for Li and Na have a global and a local energy minimum at the octahedral site, respectively. In contrast, for the heavier AM atoms, the highest energy along the path is close to the octahedral position. The migration barrier for Na is 0.53 eV, which agrees with the value obtained by Oikkonen et

DOI: 10.1021/acs.jpcc.7b03083
J. Phys. Chem. C 2017, 121, 15516−15528

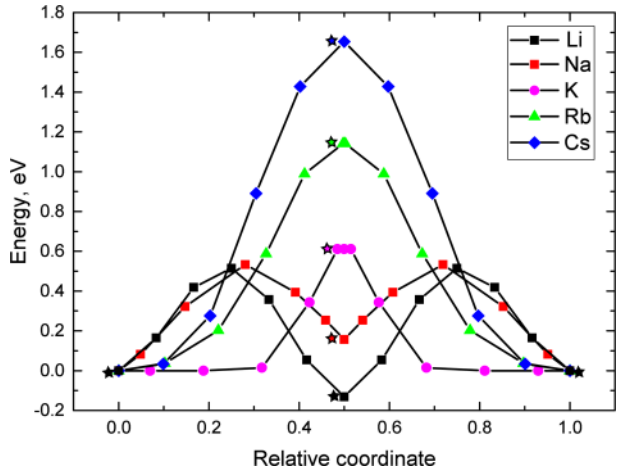

Figure 5. Migration barriers for Li, Na, K, Rb, and Cs within the interstitial diffusion mechanism. The PBE functional has been used in the CI-NEB calculation. The stars denote the barrier values calculated with the HSE06 functional using the atomic configurations determined by the PBE functional. The end points (0.0 and 1.0) of the paths correspond to two neighboring tetrahedral sites. The middle point (0.5) corresponds to the octahedral site between the two tetrahedral sites.

al.[23] The migration barrier for Li is 0.64 eV, i.e., higher by 0.11 eV than that for Na. The migration barriers for K, Rb, and Cs exhibit an increasing trend with the atomic number, i.e., 0.61, 1.14, and 1.65 eV, respectively. Here, the barrier height seems to follow fairly well the formation energy difference between the interstitials in the tetrahedral and octahedral sites, shown in Figure 2. Since the octahedral site was found to be metastable in section 3.1.2, there could exist a small dip in the energy landscape close to the peak, but this detail can also be affected by the choice of the functional.

The difference in the shape of the migration barrier between the light and heavy AM atoms can be explained by different atomic radii and different bond formation properties. The light AM elements Li and Na have small ionic radii, and therefore, they can occupy the relatively small octahedral site, create bonds with the neighboring Se atoms, and avoid strong Pauli interionic repulsion.

The migration energies for Li, Na, and K are relatively small, less than about 0.65 eV. Therefore, these atoms can also migrate via the interstitial mechanism. For Rb, a negligible migration is predicted for room temperature, while some migration can be expected at the PDT temperature. For Cs, the migration barrier is so high that appreciable diffusion is unlikely, even at the PDT temperature.

3.1.4. Alkali Metal Incorporation into the Absorber Layer. At this point, we make a short summary of our results on point defects and discuss them in the light of the existing experimental results. Especially, there is rich literature on Na incorporation into the $CuInSe_2$ absorber. For example, it is known that the Na concentration in the grain interior is less than 0.1 atom % for CIGS layers grown on soda lime glass.[10,11] Moreover, the concentration at the surface or at grain boundaries can be much higher, 10 atom % on average but locally even more than 20 atom %.[12] We are not aware of similar information on the distribution of other AM atoms. SIMS measurements show that the absorber layer can have up to 0.1 atom % of K, Rb, or Cs, but it is not clear where it is located.[3] In particular, there are no indications about the K, Rb, and Cs concentrations inside the grain.

The equilibrium impurity concentrations can be estimated for stoichiometric $CuInSe_2$ at the PDT temperature of 350 °C[2] from eq 2. For Na_{Cu}, the formation energy varies between 0.38 eV (B and C conditions) and 0.47 eV (A condition). The former results in 0.08% (0.02 atom %) of Na in the Cu sublattice sites, i.e., in a reasonable agreement with experiment. When the Na chemical potential is taken from the Na_2Se phase (A condition), this corresponds to roughly 0.004 atom % of Na. For K, Rb, and Cs, the minimum formation energies are 1.25, 1.61, and 2.12 eV, respectively. At the PDT temperature, this leads to only about 2×10^{-9} atom % of K and much less of Rb or Cs. Thus, their concentration in the grain interior of stoichiometric $CuInSe_2$ should be negligible. Li_{Cu} has an extremely low formation energy, and a very large concentration of Li_{Cu} is expected. Since the defect concentrations would no longer correspond to the dilute limit, calculating concentrations from eq 2 is not appropriate.

The attainable AM concentration depends also on kinetic factors. We found that Li, Na, and K can migrate via both the interstitial and the vacancy mechanisms. The vacancy mechanism obviously requires a high enough concentration of vacancies. Moreover, vacancies can trap interstitial AM atoms and thus limit the diffusion via the interstitial mechanism but also reduce the number of Cu vacancies available for the vacancy mechanism. Therefore, it is expected that the dominant mechanism depends strongly on the amount of Cu vacancies in the $CuInSe_2$ layer, although on the basis of our calculations we cannot estimate the borderline concentration. One should also note that the migration barrier for Cu within the vacancy mechanism (i.e., the Cu vacancy migration barrier) is quite high, 1.1 eV (the migration barrier for interstitial Cu is relatively low, 0.2 eV).[27] Irrespective of the dominant mechanism, we can conclude that Li, Na, and K diffuse relatively easily in both stoichiometric and Cu-poor $CuInSe_2$. Rb and Cs, on the other hand, can only diffuse in Cu-poor material.

Experimental results indicate that Na produces p-type conductivity in CIGS.[2,6,40,41] Nowadays, there are at least four possible explanations for this. First, the annihilation of the compensating donor defects, such as In_{Cu}.[42] Second, the enhancement of the concentration of the acceptor-type defects, such as Na_{In}.[43] Third, passivation of Se vacancies at grain boundaries through activation of oxygen atoms.[10,11] Fourth, an increase in the Cu-vacancy concentration, by Na out-diffusion during the washing up process.[15,16]

Our results for Na are in agreement with the previous studies and thus do not rule out any of the above explanations. The situation is less clear in the case of the other AM atoms,[3,15,16,22,44] but based on our calculations, we obtain trends for the AM series. Light AM atoms should enhance the processes described in the first and fourth explanations. On the basis of our bulk results of AM atoms, we cannot conclude on the third explanation. The results are largely similar for all AM atoms when considering that the only direct way to obtain increased hole concentrations is the AM atom substitution of In sites, but this could only be achieved under In-poor growth conditions and n-type samples.

On the basis of the low migration barriers, similar in- and out-diffusion of AM could happen also for Li and K. However, the low (equilibrium) concentration of K_{Cu} would limit the effect of K on the materials properties inside the grains. In the

DOI: 10.1021/acs.jpcc.7b03083
J. Phys. Chem. C 2017, 121, 15516−15528

case of Li, the formation energy is clearly lower than that for Na. This could lead to a much higher concentration of Li_{Cu}.

Experimental results indicate that heavier alkali metals displace the lighter ones.[2,3] Our results above allow us to consider what would happen when several different AM atoms are present in stoichiometric samples. We consider a situation where initially an AM atom of type A is in a Cu site and of type B is in an interstitial site. Thereafter, their positions are swapped, leading to a reaction depending on the relative stabilities of the AM atoms in the substitutional and interstitial sites

$$A_{Cu} + B_{int} \rightarrow A_{int} + B_{Cu} + \Delta H \quad (5)$$

A positive value indicates exothermic ion exchange. The reaction is also aimed to model a two-step PDT process, where the first step is carried out with the element A and the second with the element B. The reaction energies ΔH are listed in Table 2. The lower triangle corresponds to a case where the first PDT step is carried out with a lighter element than the second step. Most of the values are positive, showing that heavier elements indeed prefer to displace lighter elements into interstitial sites, which is in agreement with the experimental findings. The only outlier in the data is Cs vs K and Rb. Due to the big atomic radius of Cs, the energy difference between the interstitial and substitutional sites is small, which leads to the negative values. However, since the presence of Cs (and to a smaller extent also Rb) interstitials is expected to be small, this case may not be relevant. We also stress that, although giving probable trends, our conclusions are in principle only valid for stoichiometric $CuInSe_2$. It is most obvious that the majority of the experimentally observed ion exchange events take place close to the surface or grain boundaries or within the Cu-poor regions of the grains. We briefly speculate on the latter situation in section 3.2.4, while the former case is beyond the scope of the present study.

Table 2. Reaction Energies (in eV) for Ion Exchange As Described by Eq 5[a]

	Li	Na	K	Rb
Na	0.12	–	–	–
K	0.39	0.28	–	–
Rb	0.53	0.41	0.13	–
Cs	0.13	0.02	−0.26	−0.39

[a]Initially a lighter element A (columns) is at the Cu site and a heavier element B (rows) is at the interstitial site.

In this section, we alluded that the concentrations of AM-related defects increase when the concentration of pre-existing Cu vacancies is high. Moreover, a region with a very large concentration of AM impurities may be unstable against phase segregation and could thereby lead to formation of secondary phases. These issues will be discussed in the following section.

3.2. Secondary Phases. In this section, we consider possible mechanisms for formation of secondary phases during the PDT process, present the corresponding calculated reaction energies, and evaluate the tendency for the phases to mix or segregate with $CuInSe_2$. Once we find out which of the possible secondary phases are likely predominant, we discuss their properties to understand their effect on the device functionality and to aid in surface characterization experiments.

3.2.1. Model of the PDT Process. To investigate the possible chemical processes occurring in the CIGS solar cell absorber layer during PDT, we calculated chemical reaction enthalpies. As the kinetics in these reactions are likely very complex, at this point we do not consider reaction barriers and thus we have no access to the reaction rates. The enthalpy (ΔH) of the reaction A + B → C + D is determined by the equation

$$\Delta H = \Delta H_f(A) + \Delta H_f(B) - \Delta H_f(C) - \Delta H_f(D) \quad (6)$$

where $\Delta H_f(A)$, $\Delta H_f(B)$, $\Delta H_f(C)$, and $\Delta H_f(D)$ are the formation enthalpies of the corresponding reactants or products. Accordingly, the reaction can occur spontaneously if the difference between the total enthalpy of the reactants (A and B) and that of the products (C and D) is positive. Formation enthalpies of possible $AlkInSe_2$ compounds as calculated using the HSE06 functional are listed in Table 1.

The PDT process involves coevaporation of AM fluoride in the form of monomers and other small fragments to the surface under a Se atmosphere.[6] As a first step, we consider AM fluoride monomers reacting with Se as[18]

$$6AlkF + 4Se \rightarrow 3Alk_2Se + SeF_6 + \Delta H \quad (7)$$

The enthalpy of this reaction is 2.93, 3.95, 2.12, 1.49, and 0.27 eV for Li, Na, K, Rb, and Cs, respectively. Hence, all these reactions will occur in a Se-rich atmosphere. It has been observed that due to possible desorption, the F concentration on the CIGS surface after PDT is small,[18] and therefore, in the following we concentrate on Alk_2Se.

The next step is the reaction between the Alk_2Se and the absorber layer. To obtain the first estimate for the relative stability between Alk_2Se and $AlkInSe_2$ phases, we consider the following reaction, where AM atoms substitute Cu in $CuInSe_2$ and the Cu atoms react with the Se atmosphere to form Cu_2Se. Alternatively, one can consider In extracted from $CuInSe_2$, with Cu_2Se remaining

$$Alk_2Se + 2CuInSe_2 \rightarrow 2AlkInSe_2 + Cu_2Se + \Delta H \quad (8)$$

Formation of the $AlkInSe_2$ phase and the Cu_2Se precipitates is possible for K, Rb, and Cs with reaction enthalpies of 0.61, 0.85, and 1.10 eV, respectively. In contrast, formation of Alk_2Se is more favorable than that of $AlkInSe_2$ for Li and Na, because of negative reaction enthalpies of −0.22 and −0.21 eV, respectively. We note that this essentially depends on the In chemical potential. For instance, if we assume an equilibrium with In_2Se_3, i.e., $Alk_2Se + In_2Se_3 \rightarrow 2AlkInSe_2 + \Delta H$, we obtain positive reaction energies for all AMs, i.e., 0.94, 0.94, 1.76, 2.00, and 2.25 eV for Li, Na, K, Rb, and Cs, respectively.

If we consider the above reaction of eq 8 to proceed gradually via AM atom substitution for a small fraction of Cu only in $CuInSe_2$, this would lead to formation of the mixed phase $Alk_xCu_{(1-x)}InSe_2$ as

$$\frac{x}{2}Alk_2Se + (1-x)CuInSe_2 \rightarrow Alk_xCu_{(1-x)}InSe_2 + \frac{x}{2}Cu_2Se + \Delta H \quad (9)$$

The mixed phase is the phase with the $CuInSe_2$ crystal structure with alkali metal impurities. In contrast to it, separate phases may have different crystal structures and AM atoms agglomerate to the secondary phases, leaving the $CuInSe_2$ matrix without any changes. The energy for this reaction is in fact the same as the formation energy of the substitutional Alk_{Cu} defect in the A condition in Figure 2, because the reaction describes the substitution of a Cu atom by an AM atom. Curiously, the formation energies show that a significant

DOI: 10.1021/acs.jpcc.7b03083
J. Phys. Chem. C 2017, 121, 15516−15528

concentration of AM substitution, and thereby mixing, is only possible with Li or Na, despite the fact that these elements prefer Alk_2Se phases over $AlkInSe_2$.

3.2.2. PDT on the Cu-Deficient Region. The absorber surface is often Cu-poor already before application of PDT.[9] Reactions between the Alk_2Se and the Cu-poor layer may again lead to formation of mixed compounds, but with the AM atoms simply filling the pre-existing Cu vacancies

$$\frac{x}{2}Alk_2Se + Cu_{(1-x)}InSe_2 \rightarrow Alk_xCu_{(1-x)}InSe_2 + \frac{x}{2}Se + \Delta H \quad (10)$$

The energy of the Cu-poor compound and the energies of the compounds with small amounts of AM impurities were calculated as above, using a 128-atom supercell with one vacancy or one AM atom on the Cu site, yielding a AM concentration of $x \simeq 0.03$. eq 10 corresponds to the calculation of the formation energy of Alk_{Cu} in the A-condition, but with the Cu vacancy as the reference system. The calculated reaction enthalpies (per one AM atom) are now 0.90, 0.62, −0.20, −0.56, and −1.07 eV for Li, Na, K, Rb, and Cs, respectively. The positive values for Li and Na mean that they will readily fill all the available Cu vacancies, unless limited by the diffusion rate. For K, the value is only slightly negative, and thus, a large K concentration can be reached in the Cu-deficient region, 0.6 atom % at the PDT temperature. For Rb, this leads to about 0.001 atom % at the PDT temperature, and thus, its effect is already minor. For Cs, the concentration is negligible even at the PDT temperature. Thus, in the Cu-poor region, formation of at least a thin layer of $AlkInSe_2$ or $Alk_xCu_{(1-x)}InSe_2$ appears likely in the case of Li, Na, and K.

Irrespective of how mixed or separated phases are formed kinetically, it is useful to investigate how stable they are on given conditions. Mixed compounds can dissociate under a high PDT temperature (about 650 K) to $AlkInSe_2$ and pure $CuInSe_2$ in regions with a high concentration of AM atoms, i.e., near the surface and close to the grain boundaries.[9] To this end, we consider the reaction

$$Alk_xCu_{(1-x)}InSe_2 \rightarrow xAlkInSe_2 + (1-x)CuInSe_2 + \Delta H \quad (11)$$

Earlier, a similar reaction for the formation of the $NaInSe_2$ secondary phase was suggested by Wei et al.[20] The enthalpy of the reaction (per formula unit) for $x \simeq 0.03$ is 0.0013, 0.0102, 0.0488, 0.0637, and 0.0836 eV for Li, Na, K, Rb, and Cs, respectively. In good agreement with our model (eq 9), it was observed that K-PDT on stoichiometric CIGS leads to formation of Cu_2Se secondary phase, which was very detrimental for the device properties. However, this could be avoided by carrying out the PDT on a Cu-poor surface (eq 11).

In order to compare our results with experiments, we also have to take the mixing entropy into account and to calculate the temperature dependence of the miscibility of the $AlkInSe_2$ alloy with the CIGS layer in different proportions. We use the concept of the mixing parameter for alloys with small concentrations of a given AM and assume that the parameter is constant throughout the concentration region considered. The mixing parameter Ω is defined for an alloy by the equation

$$\Delta H_{mix} = x(1-x)\Omega \quad (12)$$

where ΔH_{mix} is the mixing enthalpy that can be explicitly evaluated from eq 11 at $x \simeq 0.03$ (corresponding to a 128-atom supercell).[45] Within the mixing parameter model of eq 12, the free energy $F(x,T)$ of the system of mixed phases can be calculated analytically as

$$F(x,T) = \Delta H_{mix}(x) - TS(x) \quad (13)$$

where T is the temperature and $S(x)$ is the entropy for a random binary alloy[46]

$$S(x) = -k_B[x\ln(x) + (1-x)\ln(1-x)] \quad (14)$$

The binodal line for the phase separation on the (x,T)-plane is obtained by requiring that the first derivative of free energy is zero. We have ignored the vibrational entropy contributions to mixing.[20,45,46] While the qualitative changes should be unaffected, small changes may arise in the case of Li and Na with small mixing enthalpies.

The binodal lines in logarithmic scale for all the AM alloys are shown in Figure 6. For a typical PDT temperature of 350 °C, mixed $Li_xCu_{(1-x)}InSe_2$ is predicted to be stable for any value of x, whereas mixed $Na_xCu_{(1-x)}InSe_2$ is stable only when $x < 10^{-3}$. At a larger x, phase segregation should take place. Experimentally, maximum Na concentrations observed are on the same order, about 0.1 atom % ($x \sim 4 \times 10^{-3}$), in a fair agreement.[9] For K, Rb, and Cs, on the other hand, mixed phases are not stable under typical PDT conditions.

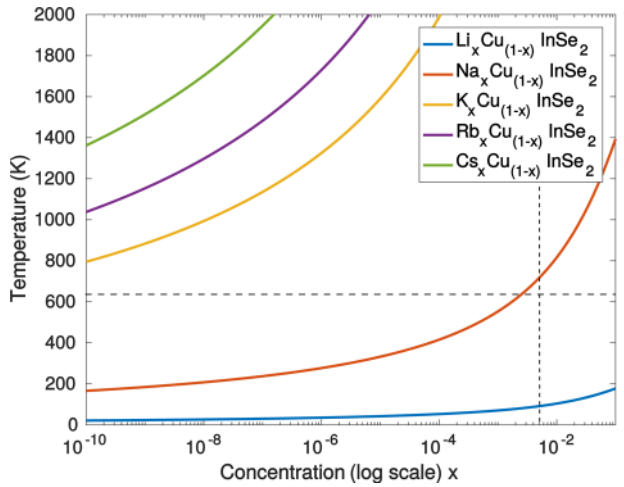

Figure 6. Phase diagram for the mixed $Alk_xCu_{(1-x)}InSe_2$ alloy. In the regions above the curves, the mixed alloys are stable, whereas the regions under the curves correspond to the coexistence of $CuInSe_2$ with the secondary phase $AlkInSe_2$. The dashed horizontal line marks a typical PDT temperature (350 °C = 623 K) and the vertical line for experimentally observed Na concentration (0.1 atom %, $x = 4 \times 10^{-3}$, ref 9), respectively.

Taking the energy for $AlkInSe_2$ in eq 11 from the chalcopyrite phase could also be a reasonable choice. For instance, Muzzillo et al. successfully grew $Cu_{(1-x)}K_xInSe_2$ alloys[47] for different values of x. For $0 < x < 0.58$, the structure was tetragonal chalcopyrite, while at $x = 1$ it was monoclinic, similarly to previous reports.[48] We found that the heat of formation for $KInSe_2$ in the chalcopyrite phase is only 0.13 eV lower than in the monoclinic phase. Such a small difference means that the binodal curve in Figure 6 is hardly affected by the adopted phase. On the other hand, it also means that due to the small energy gain, the drive toward changing the crystal structure is small. Our results suggest that the grown alloys are metastable and should eventually prefer to phase separate.

DOI: 10.1021/acs.jpcc.7b03083
J. Phys. Chem. C 2017, 121, 15516−15528

3.2.3. Structural and Electronic Properties of Secondary Phases. Atomic structures of the $AlkInSe_2$ compounds are presented in Figure 7. $LiInSe_2$ has several stable structures with

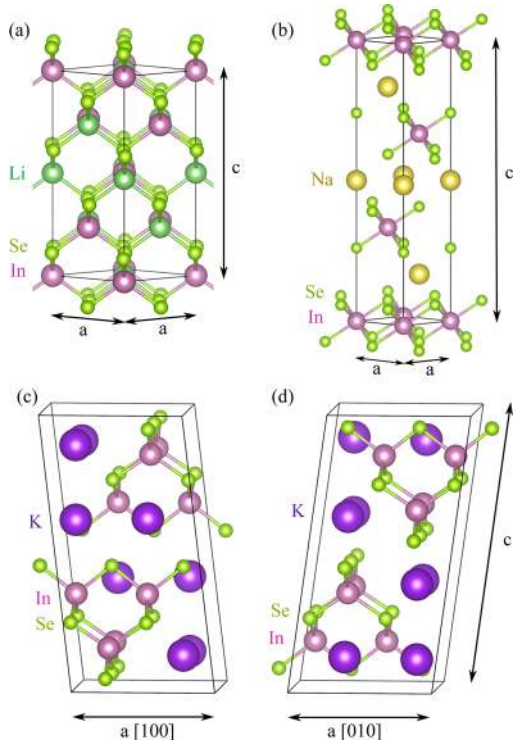

Figure 7. Atomic structures of (a) chalcopyrite $LiInSe_2$ viewed along the [110] direction; (b) delafossite $NaInSe_2$; (c) monoclinic $KInSe_2$, $RbInSe_2$, and $CsInSe_2$ viewed along the [010] direction; and (d) monoclinic $KInSe_2$, $RbInSe_2$, and $CsInSe_2$ viewed along the [100] direction. The large dark green, yellow, and violet spheres denote Li, Na, and heavier AM (K, Rb, Cs) atoms, respectively. The small light green and medium size pink spheres denote the In and Se atoms, respectively.

similar formation enthalpies, but we chose the chalcopyrite structure because it would naturally arise when substituting Cu in $CuInSe_2$ by an AM atom. Delafossite $NaInSe_2$ has a layered structure in which In is bonded to six Se atoms in an octahedral configuration (similar to, e.g., $SnSe_2$), and Na^+ ions are located in the gaps of the negatively charged $InSe_2$ layers. However, we found that the chalcopyrite structure of the $NaInSe_2$ compound is more stable, but the difference in the heat of formation is only 0.07 eV. The compounds with K, Rb, and Cs exhibit monoclinic layered structures in which In and Se atoms form chalcopyrite-like skeletons against which the AM atoms relax from the chalcopyrite Cu sites. In these monoclinic structures, the four Alk−Se bonds have slightly different lengths. Due to the similar In−Se bond arrangements, the formation enthalpies of $LiInSe_2$, $KInSe_2$, $RbInSe_2$, and $CsInSe_2$ are also similar (see Table 1).

The lattice parameters for the $AlkInSe_2$ compounds are compared with those for $CuInSe_2$ in Table 3. We find mainly a good agreement between the HSE06-calculated lattice constants and the experimental values. In addition to the same crystal structure, $LiInSe_2$ and $CuInSe_2$ have also similar experimental lattice constants, but the calculated lattice constants differ more from each others. Also, the calculated c/a ratio is only 1.96, whereas the experimental ratio is 2.03.

Table 3. Lattice Parameters (a, c), Unit Cell Volumes (Ω), and Band Gaps (E_g) for $CuInSe_2$ as Well as for $AlkInSe_2$ and Alk_2Se Compounds

compds	a (Å)	c (Å)	Ω (Å^3)	E_g (eV)
$CuInSe_2$	5.82	11.71	388.87	0.9
expt[49]	5.81	11.63	392.58	1.04
$LiInSe_2$	5.99	11.74	421.68	2.60
expt[50]	5.81	11.81	398.25	–
$NaInSe_2$	3.99	21.00	288.84	2.16
expt[51]	3.97	20.89	285.42	–
$KInSe_2$	8.19	15.85	1063.16	2.53
expt[48]	8.19	15.93	1068.52	2.68,[52] 2.71[47]
$RbInSe_2$	8.25	16.44	1118.95	2.57
expt[53]	8.34	16.64	1157.41	2.0
$CsInSe_2$	8.32	17.19	1189.93	2.66
expt[54]	8.41	17.37	1228.55	–
Cu_2Se	5.85	5.85	200.20	2.66
expt[55]	5.86	5.86	201.1	–
Li_2Se	5.97	5.97	213.2	3.85
expt[56]	6.02	6.02	217.84	–
Na_2Se	6.80	6.80	314.6	2.99
expt[56]	6.83	6.83	317.63	–
K_2Se	7.64	7.64	457.8	3.01
expt[56]	7.92	7.92	496.79	–
Rb_2Se	8.07	8.07	524.8	2.69
expt[56]	8.02	8.02	515.85	–
Cs_2Se	9.20/5.57	10.87	546.5	2.74
expt	–	–	–	–

The unit cells of $KInSe_2$, $RbInSe_2$, and $CsInSe_2$ are larger than that of $CuInSe_2$. However, as shown in Figure 7, the structures are similar to $CuInSe_2$ when viewed along the [110] direction, with a corresponding lattice constant of $5.78\sqrt{2} \approx 8.17$ Å. $KInSe_2$ has a lattice constant very close to this. The lattice constants of $RbInSe_2$ and $CsInSe_2$ are slightly larger, but should still lead to less than 2% strain. The structure of delafossite $NaInSe_2$ is rather different from the chalcopyrite $CuInSe_2$ and may thus be unlike to form also due to the incoherent interface that would be formed between the precipitate and the substrate.

The calculated band gaps are also listed in Table 3. Unfortunately, very little experimental data are available for comparison. The band gaps for $AlkInSe_2$ compounds vary between 2 and 3 eV; i.e., they are clearly larger than those for $CuInSe_2$ and $CuGaSe_2$. In support to our results, a large surface band gap of 2.52 eV has been observed experimentally by Handick et al.[22] after Na and K PDTs. Band gaps for the cubic Alk_2Se compounds are close to the band gaps for $AlkInSe_2$. If present at the absorber surface, while probably harmless for the optical properties, the AM compounds can have significant effects on the electronic characteristics of the device by introducing barriers that impede charge carrier flow or by modifying the band alignment.[57] On the other hand, they may be beneficial in passivating the $CuInSe_2$ surface or grain boundaries to prevent Cd in-diffusion or Cu out-diffusion.

3.2.4. Secondary Phases Vs Impurities. Here we summarize and compare our results concerning both AM impurities and secondary phases.

In the case of Cu-poor $CuInSe_2$, Li, Na, and K would prefer to fill the pre-existing Cu vacancies, which can lead to formation of mixed $Alk_xCu_{(1-x)}InSe_2$ compounds. Moreover, the migration barriers for the vacancy mechanism are relatively low for all the AM atoms. We predict that the mixed phase of

DOI: 10.1021/acs.jpcc.7b03083
J. Phys. Chem. C 2017, 121, 15516−15528

$Alk_xCu_{(1-x)}InSe_2$ compounds is stable for Na with $x \leq 0.1$ atom % and for Li with all x values under typical PDT conditions. Since the Alk_2Se compound tends to be more stable than $AlkInSe_2$ for Na and especially for Li, even if $AlkInSe_2$ is formed, it may reduce to Alk_2Se (eq 8). This could consequently lead to formation of In-rich/Cu-poor phases.

In the case of K, Rb, and Cs, phase separation is expected. This view is based on total energy calculations of the bulk phases and on the high formation energies of the related defects in both the stoichiometric and Cu-deficient regions. It is not clear how deep in the Cu-poor phase AM atoms can diffuse and what their concentrations are before phase separation starts to take place. Consequently, since $AlkInSe_2$ leads to a lower AM chemical potential than Alk_2Se, the supply of AM atoms inside the grain diminishes and the formation energies of AM defects increase. That is, $AlkInSe_2$ passivates the surface. Moreover, if the phase separation occurs so that excess Cu is pushed deeper into the grain and the ensuing vacancies are filled with AM atoms, this would decrease the Cu deficiency in the grain interior.

In the case of stoichiometric $CuInSe_2$, secondary phase formation may take place right at the surface, where energetics can differ from that in the bulk. We think that the AM concentrations inside grains should follow more closely to those predicted from the formation energies. Only Li, Na, and K have migration barriers low enough to allow diffusion deeper into the grains.

With all this information at hand, we can speculate on what would happen in grains which are Cu deficit at the outer regions and nearly stoichiometric in the interior. As mentioned above, all the AM atoms can diffuse in the Cu-poor region and there also their formation energies are low. Consequently, there should be AM atom influx, at least when assuming that secondary phase formation at the surface is avoided. On the other hand, diffusion of AM atoms from the Cu-poor region to the stoichiometric region becomes limited by the fact that the formation energy for an AM atom at the Cu site is much lower than that at the interstitial site. Consequently, AM atoms would accumulate in Cu sites near the boundary between the Cu-depleted region and the almost-stoichiometric CIGS. The concentration profile of the AM elements reported by Jackson et al.[3] supports this idea.

Putting it all together, (i) Li and Na can behave as impurities at significant concentrations anywhere in the grains of the absorber material. They have low formation energies at the Cu site and at the interstitial sites and low migration barriers. At higher concentrations, they can remain in the mixed phase instead of forming secondary phases. (ii) K, Rb, and Cs have stronger tendencies toward formation of secondary phases, as evidenced by the binodal line (or high defect formation energies) and the overall low heats of formation in comparison with the competing phases. The process may occur at the surface, or after sufficient absorption of AM into the Cu-poor region, which can occur since the formation energies at the pre-existing Cu vacancies are low and the AM atoms can migrate via the vacancy mechanism.

Thus, our results support the notion that different AM atoms can have different effects on the improvement of the solar cell characteristics.[3] In the ref 3, the best devices were obtained by the RbF PDT process for absorbers on SLG (containing Na). We propose that lighter elements behave as impurities and contribute to the increased p-type doping, while the heavier elements are more prone to forming secondary phases that can passivate the surface.

4. CONCLUSIONS

The latest efficiency improvements in thin-film CIGS solar cells are obtained by evaporation of AM atoms, typically AM fluorides, on the CIGS surface. According to experimental evidence, light and heavy AM atoms affect the properties of the CIGS material via different types of processes. In the present work, we studied effects of AM atoms (Li, Na, K, Rb, and Cs) in the $CuInSe_2$ grain interior. We calculated the formation and migration energies of the AM impurities and the heats of formation of several secondary phases that can be formed during the AM-PDT. On the basis of our results, we proposed a model for the PDT process and discussed the temperature-dependent solubilities of $AlkInSe_2$ secondary phases in the bulk $CuInSe_2$.

The light AM atoms Na and Li act as impurities in the grain interior, in contrast to the heavier AM atoms, K, Rb, and Cs, which favor formation of secondary phases expected to occur initially at grain boundaries or close to the surface. The effect of an AM impurity on the electronic structure of the absorber depends on its composition. For instance, substitutional Alk_{In} impurities have low formation energies at In-poor conditions and can act as acceptors, whereas AM impurities in other sites are donors or electrically neutral. Our findings are supported by experimental results for concentrations of AM atoms and their migration barriers.

In addition to acting as substitutional impurities, AM atoms may affect the structure of the absorber through different kinetic processes. AM atoms prefer to migrate via the vacancy mechanism, while light AM elements can move via the interstitial mechanism also. Moreover, the migration barriers do not increase monotonously from Li to Cs. The trends predicted reflect the decrease of the tendency to make chemical bonds and the increase in the ionic radius toward heavier AM atoms. In order to reach final conclusions about the preferable migration mechanism in the actual absorber material, more information about AM atom migration barriers at the grain boundaries and inside the Cu-poor phase is required.

On the basis of the calculated heats of formation and the free energy of mixing, Li and Na are found to form mixed phases with $CuInSe_2$, whereas K, Rb, and Cs have a stronger tendency toward formation of secondary phases in the form of $AlkInSe_2$. We suggest that these can lead to passivation of the surface and the grain boundaries, by hindering the diffusion of elements in the Cu sublattice, and modification of the electronic structure by the wide band gap of these phases.

Our work shows that the light (Li, Na) and heavy (Rb, Cs) AM atoms have distinct effects on the structure of the absorber. K is in between and may partially serve in both roles. Once the absorber atomic structures are known, the next step is to assess their effect on absorber properties (such as electrical conductivity, absorbance, and carrier life times) and the solar cell performance as a whole.

AUTHOR INFORMATION

Corresponding Author

*E-mail: martti.puska@aalto.fi.

ORCID

H.-P. Komsa: 0000-0002-0970-0957

M. J. Puska: 0000-0002-8419-3289

DOI: 10.1021/acs.jpcc.7b03083
J. Phys. Chem. C 2017, 121, 15516−15528

Notes

The authors declare no competing financial interest.

■ ACKNOWLEDGMENTS

The project has received funding from the European Unions Horizon 2020 research and innovation program under the grant agreement No. 641004 (Sharc 25). H.P.K. also thanks the Academy of Finland for the support under Project No. 286279 and through its Centres of Excellence Programme (2012-2017) under Project No. 251748. We acknowledge the generous computational resources provided by the CSC supercomputer center of Finland and also by the Aalto Science-IT project. The authors would also like to thank Dr. Wolfram Witte, Dr. Dimitrios Hariskos, Dr. Philip Jackson, and Dr. Roland Würz from ZSW and Dr. Stephan Bücheler from EMPA for discussions on CIGS solar cell manufacturing processes.

■ REFERENCES

(1) Herrmann, D.; Kratzert, P.; Weeke, S.; Zimmer, M.; Djordjevic-Reiss, J.; Hunger, R.; Lindberg, P.; Wallin, E.; Lundberg, O.; Tolt, L. CIGS module manufacturing with high deposition rates and efficiencies. *2014 IEEE 40th Photovoltaic Specialist Conference*; IEEE, 2014; pp 2775−2777.

(2) Reinhard, P.; Bissig, B.; Pianezzi, F.; Avancini, E.; Hagendorfer, H.; Keller, D.; Fuchs, P.; Döbeli, M.; Vigo, C.; Crivelli, P.; et al. Features of KF and NaF postdeposition treatments of $Cu(In,Ga)Se_2$ absorbers for high efficiency thin film solar cells. *Chem. Mater.* **2015**, *27*, 5755−5764.

(3) Jackson, P.; Wuerz, R.; Hariskos, D.; Lotter, E.; Witte, W.; Powalla, M. Effects of heavy alkali elements in $Cu(In,Ga)Se_2$ solar cells with efficiencies up to 22.6%. *Phys. Status Solidi RRL* **2016**, *10*, 583−586.

(4) Abou-Ras, D.; Wagner, S.; Stanbery, B. J.; Schock, H.-W.; Scheer, R.; Stolt, L.; Siebentritt, S.; Lincot, D.; Eberspacher, C.; Kushiya, K. Innovation highway: Breakthrough milestones and key developments in chalcopyrite photovoltaics from a retrospective viewpoint. *Thin Solid Films* **2017**, *633*, 2.

(5) Jackson, P.; Hariskos, D.; Wuerz, R.; Wischmann, W.; Powalla, M. Compositional investigation of potassium doped $Cu(In,Ga)Se_2$ solar cells with efficiencies up to 20.8%. *Phys. Status Solidi RRL* **2014**, *8*, 219−222.

(6) Rudmann, D.; da Cunha, A. F.; Kaelin, M.; Kurdesau, F.; Zogg, H.; Tiwari, A. N.; Bilger, G. Efficiency enhancement of $Cu(In,Ga)Se_2$ solar cells due to post-deposition Na incorporation. *Appl. Phys. Lett.* **2004**, *84*, 1129−1131.

(7) Jackson, P.; Hariskos, D.; Wuerz, R.; Kiowski, O.; Bauer, A.; Friedlmeier, T. M.; Powalla, M. Properties of $Cu(In,Ga)Se_2$ solar cells with new record efficiencies up to 21.7%. *Phys. Status Solidi RRL* **2015**, *9*, 28−31.

(8) Repins, I.; Contreras, M. A.; Egaas, B.; DeHart, C.; Scharf, J.; Perkins, C. L.; To, B.; Noufi, R. 19,9%-efficient $ZnO/CdS/CuInGaSe_2$ solar cell with 81,2% fill factor. *Prog. Photovoltaics* **2008**, *16*, 235−239.

(9) Pianezzi, F.; Reinhard, P.; Chirila, A.; Bissig, B.; Nishiwaki, S.; Buecheler, S.; Tiwari, A. N. Unveiling the effects of post-deposition treatment with different alkaline elements on the electronic properties of CIGS thin film solar cells. *Phys. Chem. Chem. Phys.* **2014**, *16*, 8843−8851.

(10) Cojocaru-Mirédin, O.; Schwarz, T.; Choi, P.; Herbig, M.; Wuerz, R.; Raabe, D. Atom Probe Tomography Studies on the $Cu(In,Ga)Se_2$ Grain Boundaries. *J. Visualized Exp.* **2013**, *74*, e50376.

(11) Couzinie-Devy, F.; Cadel, E.; Barreau, N.; Arzel, L.; Pareige, P. Atom probe study of Cu-poor to Cu-rich transition during Cu(In,Ga)Se2 growth. *Appl. Phys. Lett.* **2011**, *99*, 232108.

(12) Cojocaru-Mirédin, O.; Choi, P.; Wuerz, R.; Raabe, D. Exploring the p−n junction region in $Cu(In,Ga)Se_2$ thin-film solar cells at the nanometer-scale. *Appl. Phys. Lett.* **2012**, *101*, 181603.

(13) Contreras, M. A.; Egaas, B.; Ramanathan, K.; Hiltner, J.; Swartzlander, A.; Hasoon, F.; Noufi, R. Progress toward 20% efficiency in $Cu(In,Ga)Se_2$ polycrystalline thin-film solar cells. *Prog. Photovoltaics* **1999**, *7*, 311−316.

(14) Hetzer, M. J.; Strzhemechny, Y. M.; Gao, M.; Contreras, M. A.; Zunger, A.; Brillson, L. J. Direct observation of copper depletion and potential changes at copper indium gallium diselenide grain boundaries. *Appl. Phys. Lett.* **2005**, *86*, 162105.

(15) Maeda, T.; Kawabata, A.; Wada, T. First-principles study on alkali-metal effect of Li, Na, and K in $CuInSe_2$ and $CuGaSe_2$. *Jpn. J. Appl. Phys.* **2015**, *54*, 08KC20.

(16) Yuan, Z.-K.; Chen, S.; Xie, Y.; Park, J.-S.; Xiang, H.; Gong, X.-G.; Wei, S.-H. Na-diffusion enhanced p-type conductivity in $Cu(In,Ga)Se_2$: A new mechanism for efficient doping in semiconductors. *Adv. Energy Mater.* **2016**, *6*, 1601191.

(17) Zellner, M. B.; Birkmire, R. W.; Eser, E.; Shafarman, W. N.; Chen, J. G. Determination of activation barriers for the diffusion of sodium through CIGS thin-film solar cells. *Prog. Photovoltaics* **2003**, *11*, 543−548.

(18) Laemmle, A.; Wuerz, R.; Schwarz, T.; Cojocaru-Miredin, O.; Choi, P.-P.; Powalla, M. Investigation of the diffusion behavior of sodium in $Cu(In,Ga)Se_2$ layers. *J. Appl. Phys.* **2014**, *115*, 154501.

(19) Bastek, J. Fremd- und Selbstdiffusion in Duennschichtsolarzellen auf der Basis mehrkomponentiger Halbleiterverbindungen. Ph.D. thesis, Westfaelische Wilhelms-Universitaet, Muenster, 2013.

(20) Wei, S.-H.; Zhang, S. B.; Zunger, A. Effects of Na on the electrical and structural properties of $CuInSe_2$. *J. Appl. Phys.* **1999**, *85*, 7214−7218.

(21) Klein, A.; Loher, T.; Pettenkofer, C.; Jaegermann, W. Chemical interaction of Na with cleaved (011) surfaces of $CuInSe_2$. *J. Appl. Phys.* **1996**, *80*, 5039−5043.

(22) Handick, E.; Reinhard, P.; Alsmeier, J.-H.; Köhler, L.; Pianezzi, F.; Krause, S.; Gorgoi, M.; Ikenaga, E.; Koch, N.; Wilks, R. G.; et al. Potassium postdeposition treatment-induced band gap widening at $Cu(In,Ga)Se_2$ surfaces - reason for performance leap? *ACS Appl. Mater. Interfaces* **2015**, *7*, 27414−27420.

(23) Oikkonen, L. E.; Ganchenkova, M. G.; Seitsonen, A. P.; Nieminen, R. M. Effect of sodium incorporation into $CuInSe_2$ from first principles. *J. Appl. Phys.* **2013**, *114*, 083503.

(24) Ghorbani, E.; Kiss, J.; Mirhosseini, H.; Roma, G.; Schmidt, M.; Windeln, J.; Kühne, T. D.; Felser, C. Hybrid-functional calculations on the incorporation of Na and K impurities into the $CuInSe_2$ and $CuIn_5Se_8$ solar-cell materials. *J. Phys. Chem. C* **2015**, *119*, 25197−25203.

(25) Liao, D.; Rockett, A. Cu depletion at the $CuInSe_2$ surface. *Appl. Phys. Lett.* **2003**, *82*, 2829−2831.

(26) Zhang, S. B.; Wei, S.-H.; Zunger, A. Stabilization of ternary compounds via ordered arrays of defect pairs. *Phys. Rev. Lett.* **1997**, *78*, 4059−4062.

(27) Oikkonen, L. E.; Ganchenkova, M. G.; Seitsonen, A. P.; Nieminen, R. M. Mass transport in $CuInSe_2$ from first principles. *J. Appl. Phys.* **2013**, *113*, 133510.

(28) Van de Walle, C. G.; Laks, D. B.; Neumark, G. F.; Pantelides, S. T. First-principles calculations of solubilities and doping limits: Li, Na, and N in ZnSe. *Phys. Rev. B: Condens. Matter Mater. Phys.* **1993**, *47*, 9425−9434.

(29) Kresse, G.; Furthmüller, J. Efficient iterative schemes for *ab initio* total-energy calculations using a plane-wave basis set. *Phys. Rev. B: Condens. Matter Mater. Phys.* **1996**, *54*, 11169−11186.

(30) Kresse, G.; Furthmüller, J. Efficiency of *ab initio* total energy calculations for metals and semiconductors using a plane-wave basis set. *Comput. Mater. Sci.* **1996**, *6*, 15−50.

(31) Malitckaya, M.; Komsa, H.-P.; Havu, V.; Puska, M. J. First-principles modeling of point defects and complexes in thin-film solar-cell absorber $CuInSe_2$. *Advanced Electronic Materials* **2017**, *3*, 1600353.

(32) Freysoldt, C.; Neugebauer, J.; Van de Walle, C. G. Electrostatic interactions between charged defects in supercells. *Phys. Status Solidi B* **2011**, *248*, 1067−1076.

DOI: 10.1021/acs.jpcc.7b03083
J. Phys. Chem. C 2017, 121, 15516−15528

(33) Komsa, H.-P.; Rantala, T. T.; Pasquarello, A. Finite-size supercell correction schemes for charged defect calculations. *Phys. Rev. B: Condens. Matter Mater. Phys.* **2012**, *86*, 045112.
(34) Heyd, J.; Scuseria, G. E.; Ernzerhof, M. Hybrid functionals based on a screened Coulomb potential. *J. Chem. Phys.* **2003**, *118*, 8207−8215.
(35) Henkelman, G.; Jónsson, H. Improved tangent estimate in the nudged elastic band method for finding minimum energy paths and saddle points. *J. Chem. Phys.* **2000**, *113*, 9978−9985.
(36) Pohl, J.; Albe, K. Intrinsic point defects in $CuInSe_2$ and $CuGaSe_2$ as seen via screened-exchange hybrid density functional theory. *Phys. Rev. B: Condens. Matter Mater. Phys.* **2013**, *87*, 245203.
(37) Cahen, D.; Noufi, R. Free energies and enthalpies of possible gas phase and surface reactions for preparation of $CuInSe_2$. *J. Phys. Chem. Solids* **1992**, *53*, 991−1005.
(38) Oikkonen, L. E.; Ganchenkova, M. G.; Seitsonen, A. P.; Nieminen, R. M. Formation, migration, and clustering of point defects in $CuInSe_2$ from first principles. *J. Phys.: Condens. Matter* **2014**, *26*, 345501.
(39) Siebentritt, S.; Igalson, M.; Persson, C.; Lany, S. The electronic structure of chalcopyrites - bands, point defects and grain boundaries. *Prog. Photovoltaics* **2010**, *18*, 390−410.
(40) Shafarman, W. N.; Siebentritt, S.; Stolt, L. In *Handbook of Photovoltaic Science and Engineering*; John Wiley & Sons, Ltd, 2011; pp 546−599.
(41) Lammer, M.; Klemm, U.; Powalla, M. Sodium co-evaporation for low temperature $Cu(In,Ga)Se_2$ deposition. *Thin Solid Films* **2001**, *387*, 33−36. Proceeedings of Symposium N on Thin Film Photovoltaicmaterials of the E-MRS Spring Conference.
(42) Contreras, M. A.; Egaas, B.; Dippo, P.; Webb, J.; Granata, J.; Ramanathan, K.; Asher, S.; Swartzlander, A.; Noufi, R. On the role of Na and modifications to $Cu(In,Ga)Se_2$ absorber materials using thin-MF (M = Na, K, Cs) precursor layers [solar cells]. *1997 IEEE 26th Photovoltaic Specialists Conference*; IEEE, 1997; pp 359−362.
(43) Niles, D. W.; Al-Jassim, M.; Ramanathan, K. Direct observation of Na and O impurities at grain surfaces of $CuInSe_2$ thin films. *J. Vac. Sci. Technol., A* **1999**, *17*, 291−296.
(44) Pianezzi, F.; Reinhard, P.; Chirilă, A.; Nishiwaki, S.; Bissig, B.; Buecheler, S.; Tiwari, A. N. Defect formation in $Cu(In,Ga)Se_2$ thin films due to the presence of potassium during growth by low temperature co-evaporation process. *J. Appl. Phys.* **2013**, *114*, 194508.
(45) Garidel, P.; Johann, C.; Blume, A. The calculation of heat capacity curves and phase diagrams based on regular solution theory. *J. Therm. Anal. Calorim.* **2005**, *82*, 447−455.
(46) Alling, B.; Hogberg, H.; Armiento, R.; Rosen, J.; Hultman, L. A theoretical investigation of mixing thermodynamics, age-hardening potential, and electronic structure of ternary M11-xM2xB2 alloys with AlB2 type structure. *Sci. Rep.* **2015**, *5*, 9888.
(47) Muzzillo, C. P.; Mansfield, L. M.; Ramanathan, K.; Anderson, T. J. Properties of Cu1-xKxInSe$_2$ alloys. *J. Mater. Sci.* **2016**, *51*, 6812−6823.
(48) Wang, P.; Huang, X.-Y.; Liu, Y.-L.; Wei, Y.-G.; Li, J.; Guo, H.-Y. Solid state synthesis at intermediate temperature and structural characterization of $KInSe_2$. *Hua Hsueh Hsueh Pao* **2000**, *58*, 1005−1008.
(49) Maeda, T.; Takahiro, W. Electronic structure and characteristics of chemical bonds in $CuInSe_2$, $CuGaSe_2$ and $CuAlSe_2$. *Extended Abstracts of the 2009 International Conference on Solid State Devices and Materials*; 2009; pp 1270−1271.
(50) Beister, H. J.; Ves, S.; Hönle, W.; Syassen, K.; Kühn, G. Structural phase transitions and optical absorption of $LiInSe_2$ under pressure. *Phys. Rev. B: Condens. Matter Mater. Phys.* **1991**, *43*, 9635−9642.
(51) Hoppe, R.; Lidecke, W.; Frorath, F. Zur Kenntnis von $NaInS_2$ und $NaInSe_2$. *Z. Anorg. Allg. Chem.* **1961**, *309*, 49−54.
(52) Kish, Z.; Lazarev, V. B.; Peresh, E.; Semrad, E. Compounds in In_2Se_3−K_2Se. *Neorg Mater.* **1988**, *24*, 1602−1605.
(53) Huang, F. Q.; Deng, B.; Ellis, D. E.; Ibers, J. A. Preparation, structures, and band gaps of $RbInS_2$ and $RbInSe_2$. *J. Solid State Chem.* **2005**, *178*, 2128−2132.
(54) Ward, M. D.; Pozzi, E. A.; Van Duyne, R. P.; Ibers, J. A. Syntheses, structures, and optical properties of the indium/germanium selenides $Cs_4In_8GeSe_{16}$, $CsInSe_2$, and $CsInGeSe_4$. *J. Solid State Chem.* **2014**, *212*, 191−196.
(55) Gulay, L.; Daszkiewicz, M.; Strok, O.; Pietraszko, A. Crystal Structure of Cu_2Se. *Chem. Mater. Alloys* **2011**, 200−205.
(56) AlayeAbbas, S.; Sabir, N.; Saeed, Y.; Shaukat, A. Electronic and optical properties of alkali metal selenides in anti-CaF_2 crystal structure from first-principles. *J. Alloys Compd.* **2010**, *503*, 10−18.
(57) Goddard, W. A. Predicted roles of defects on band offsets and energetics at CIGS ($Cu(In,Ga)Se_2$/CdS) solar cell interfaces and implications for improving performance. *J. Chem. Phys.* **2014**, *141*, 094701.

DOI: 10.1021/acs.jpcc.7b03083
J. Phys. Chem. C 2017, 121, 15516−15528